



Geophysical Research Letters

RESEARCH LETTER

10.1029/2020GL088312

Key Points:

- The derived vertical evolution of clouds from FY-4A shows great correspondence with DPR vertical structures of precipitation
- Synergistic application of passive and active satellite sensors offers a panoramic view of the in-cloud microphysical process

Supporting Information:

- Supporting Information S1

Correspondence to:

A. Zhang,
zhangaoq3@mail.sysu.edu.cn

Citation:

Chen, Y., Li, W., Chen, S., Zhang, A., & Fu, Y. (2020). Linkage between the vertical evolution of clouds and droplet growth modes as seen from FY-4A AGRI and GPM DPR. *Geophysical Research Letters*, 47, e2020GL088312. <https://doi.org/10.1029/2020GL088312>

Received 7 APR 2020

Accepted 14 JUL 2020

Accepted article online 19 JUL 2020

Linkage Between the Vertical Evolution of Clouds and Droplet Growth Modes as Seen From FY-4A AGRI and GPM DPR

Yilun Chen^{1,2} , Weibiao Li^{1,2} , Shumin Chen^{1,2} , Aoqi Zhang^{1,2} , and Yunfei Fu³

¹School of Atmospheric Sciences, Sun Yat-sen University, Zhuhai, China, ²Southern Marine Science and Engineering Guangdong Laboratory (Zhuhai), Zhuhai, China, ³School of Earth and Space Sciences, University of Science and Technology of China, Hefei, China

Abstract Based on matched scans from the FY-4A satellite's Advanced Geostationary Radiation Imager (AGRI) and the NASA/JAXA Global Precipitation Measurement (GPM) Core Observatory's Dual-frequency Precipitation Radar (DPR), the microphysical mechanisms of the derived vertical evolution of cloud effective radius (R_e) and its correspondence with precipitation droplet growth modes are revealed in this study. The results show that there were two turning points in the R_e vertical evolution, which divided the R_e profile into solid-phase, mixed-phase, and liquid-phase zones from top to bottom. There were also two turning points in the upper layer of DPR reflectivity, which showed good correspondence with R_e turning points in both height and physical sense. The main droplet growth modes in the three zones are nucleation/glaciation, deposition, and riming, respectively. The linkage between R_e vertical evolution and droplet growth modes would be useful in real-time monitoring of cloud microphysical processes.

1. Introduction

The vertical evolution of precipitating clouds indicates the processes of movement, transformation, and phase change of water vapor, cloud particles, and precipitation droplets and is key to revealing the physical nature of these clouds and improving precipitation predictions (Houze et al., 2015; Rosenfeld, Andreae, et al., 2014). There are potentially numerous liquid cloud and supercooled water vapor particles within clouds below temperatures of 0°C. This not only affects our accurate understanding of cloud microphysics but threatens flight safety, due to the possibility of aircraft icing (Caliskan & Hajiyev, 2013; Fu, 2014).

The limitations of ground-based observations and model simulations mean that satellite observations have been exerting a continuously growing impact on researches of cloud vertical evolution (Geer et al., 2017). Since the 1990s, several satellites have been launched with instruments to detect the vertical structures of cloud and precipitation. For instance, the Cloud Profiling Radar (CPR) onboard CloudSat can accurately retrieve the effective radius (R_e) and water content of cloud particles within each vertical layer (Stephens et al., 2002), which has been widely used for studying the vertical structures of clouds (Stephens et al., 2008); the Cloud-Aerosol LIDAR with Orthogonal Polarization (CALIOP) detects high-resolution reflectivity profiles of the cloud top and is applied in studying the cloud microphysics of cirrus clouds (Chen & Fu, 2018; Winker et al., 2009); and satellite precipitation radars, including the Tropical Rainfall Measuring Mission (TRMM) Precipitation Radar (PR) and the Global Precipitation Measurement (GPM) Dual-frequency Precipitation Radar (DPR), provide three-dimensional information about rain rate and droplet size distribution (DSD) for precipitation studies (Awaka et al., 2009; Iguchi et al., 2012). However, despite the diversity and high detection accuracy of these active instruments, they all work on low Earth orbits with a narrow scanning swath and long revisit period, which mean they are limited in continuous monitoring and cannot meet the needs of severe weather warning systems.

Compared with those active instruments, passive visible and infrared instruments are much more common and are carried on various meteorological satellites. Using multiple near-infrared channels and weighting functions, Platnick (2000) attempted to directly retrieve the vertical evolution of cloud parameters, but the application of this method is restricted by high requirements on cloud uniformity and channel sensitivity (King & Vaughan, 2012). Currently, using bispectral reflectance (BSR) to obtain the cloud-top R_e and establishing the relationship between R_e and cloud-top temperature (or height) is the key method for indicating

the vertical evolution of clouds (Ansmann et al., 2008; Campos Braga et al., 2017; Rosenfeld & Lensky, 1998; Zheng & Rosenfeld, 2015). This method relies on two core assumptions: (1) all cloud pixels in a certain region have similar R_e -Temperature function ($R_e(T)$), so that $R_e(T)$ of a single pixel is identical to composite $R_e(T)$ within this region; (2) R_e near the cloud top is similar to that inside the cloud at the same height.

The vertical evolution of clouds derived from passive satellite instruments has been used in a wide range of microphysical studies. For instance, the shape of $R_e(T)$ was used to identify five microphysical zones of different dominant cloud microprocesses (Rosenfeld & Woodley, 2003). Using matched observations from the TRMM Visible and Infrared Scanner (VIRS) and PR, the anthropogenic aerosols suppressing precipitation were observed and attributed to greatly reduced R_e (Rosenfeld et al., 2007). $R_e(T)$ was also applied in studying the impacts of aerosols on clouds' glaciation temperature and mixed-phase precipitation, the vertical micro-physics of severe convective storms, and other studies about cloud-aerosol-precipitation properties (Rudich et al., 2002; Woodley et al., 2008).

These previous studies have laid a good foundation for studying cloud microstructures. However, the linkage between cloud particle microphysics and precipitation droplet growth is still unclear and worthy of further investigation. In addition, the application of instruments for measuring $R_e(T)$ on geostationary satellites is still rare (Lensky & Rosenfeld, 2006), hampering efforts for continuous or real-time monitoring of the vertical evolution of clouds. China's last-generation FY-2 series lacked near-infrared channels around the 2 μm wavelength, which resulted in huge uncertainty in the retrieved cloud parameters. Fortunately, this shortcoming has been resolved in the latest FY-4A geostationary satellite (Yang et al., 2017). Recently, we developed a method for retrieving the vertical evolution of R_e based on the FY-4A Advanced Geostationary Radiation Imager (AGRI) (Chen et al., 2020), although further validations are urgently needed (for instance, whether this algorithm is suitable for snowfall clouds in winter).

In this manuscript, we focused on a disastrous rainfall-blizzard event around Wuhan, in China's Hubei province, in February 2020. Based on the matched detections from FY-4A AGRI and GPM DPR, we could recognize the relationship between various cloud particle microphysics and precipitation droplet growth modes, which can provide a scientific basis for real-time monitoring of cloud and precipitation microphysics using geostationary observations.

2. Data and Methods

FY-4A was launched in 2016 with a central longitude of 104.7°E (Yang et al., 2017). After several calibrations, it started operation in 2018, and data were released by FENGYUN Satellite Data Center (<http://data.nsmc.org.cn>). The AGRI onboard FY-4A scans the Earth on 14 channels, among which the visible channels (centered at 0.47, 0.65, and 0.825 μm) have a resolution of 1 km, the near-infrared channels (centered at 1.375, 1.61, 2.225, and 3.75 μm) have a resolution of 2 km, and the resolution of the infrared bands is 4 km (centered at 3.75, 6.25, 7.1, 8.5, 10.8, 12.0, and 13.5 μm). AGRI can perform disk scans as fast as every 15 min, which is effective for tracking clouds. Currently, there are some official products based on AGRI observations, such as cloud mask and cloud-top height (Min et al., 2017). In this study, we used Level 1 AGRI data at the 0.65, 1.61, and 10.8 μm channels, and Geo data, including solar zenith, satellite zenith, and relative azimuth. We also used a cloud-top height official product with 4 km resolution.

Recently, we developed a retrieval algorithm of R_e vertical evolution based on FY-4A AGRI, which was applied in this study with slight modifications. First, a BSR lookup table was established using 0.65 and 1.61 μm reflectance for retrieving cloud-top R_e ; then the R_e profile in a certain region was established by combining the R_e and the cloud-top height at each pixel. The retrieved cloud-top R_e has a correlation coefficient of over 0.9 with MODIS R_e (Chen et al., 2020). After establishing the relationship between R_e and cloud-top height, we calculated the 25th, 50th, and 75th percentiles of R_e at each 0.25 km interval with a sample size greater than 150. Otherwise the percentiles would not be given, to eliminate errors caused by extreme values.

GPM DPR is the first spaceborne dual-frequency precipitation radar to contain a Ku-band radar (KuPR, 13.6 GHz) and a Ka-band radar (KaPR, 35.5 GHz). KuPR works in normal scan (NS) mode with 49 pixels per track, which is similar to TRMM PR. KaPR has two scan modes including a matched scan (MS) mode on the central 25 pixels of NS track, and a high-sensitivity scan (HS) mode on the outer 24 pixels of NS track (after 21 May 2018). Based on the different responses of Ku- and Ka-band echoes to hydrometers, the GPM

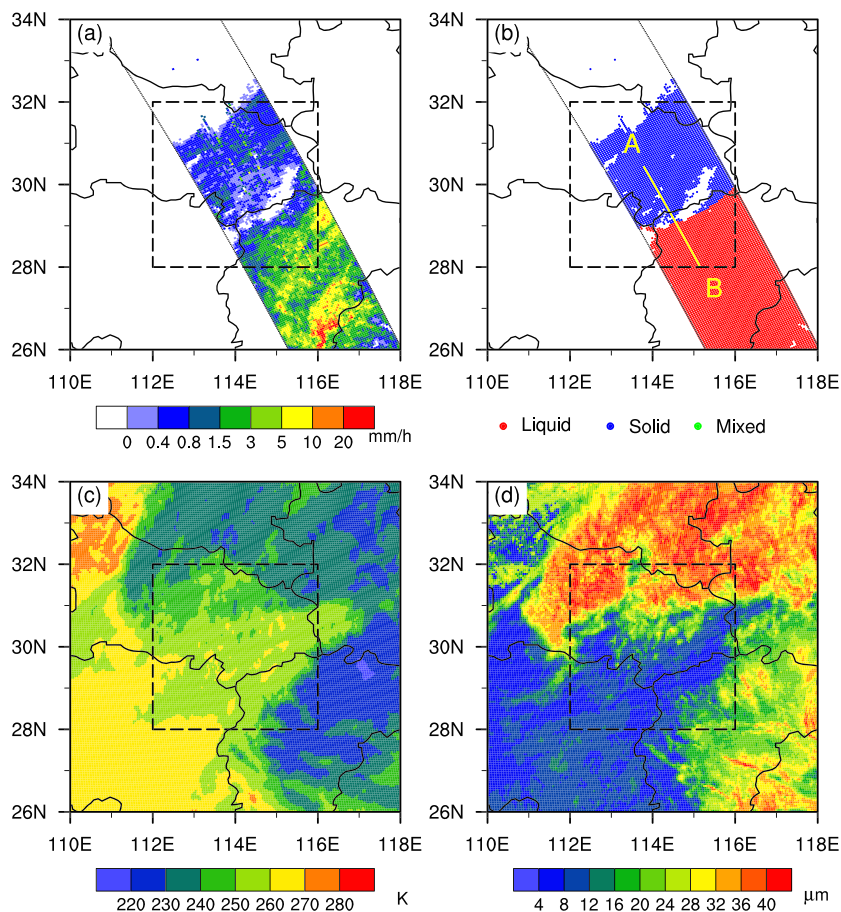


Figure 1. Horizontal distributions of the rainfall-blizzard event on 15 February 2020: GPM DPR (a) near-surface rain rate and (b) near-surface precipitation phase, (c) FY-4A AGRI 10.8 μm brightness temperature, and (d) the retrieved R_e . The dashed rectangle indicates our study region.

precipitation processing system provides a dual-frequency precipitation product, 2ADPR (Iguchi et al., 2012). In this study, the precipitation information mainly comes from 2ADPR on NS tracks (Ku-band reflectivity, near-surface rain rate, etc.) and MS tracks (DSD profiles) with a horizontal resolution of 5 km and a vertical interval of 125 m.

3. Results

On 15 February 2020, a disastrous rainfall-blizzard event brought by a cold front swept through Wuhan and the surrounding area. The strong winds, rapid cooling, and road icing that accompanied this event caused extremely adverse effects for the contemporaneous epidemic control and material transportation in the region (Sun et al., 2020).

GPM DPR happened to capture this event at 0744 UTC, when the cold front had moved southeasterly to the southeast of the study region (supporting information Figure S1). In the lower right of the study region (the dashed rectangle in Figure 1), near-surface precipitation mainly appeared in its liquid phase, accounting for around one third of the total precipitation pixels with a central rain rate of 5–10 mm/hr (Figures 1a and 1b). In the top left area of the study region, near-surface precipitation appeared as snowfall, accounting for about two-thirds of the total pixels, with central intensity reaching 0.8 mm/hr (Figures 1a and 1b).

Figure 1c shows the 10.8 μm brightness temperature, which indicates the temperature on an object's surface, at 0730 UTC on 15 February 2020 from FY-4A. The study region was completely covered by clouds at the time, with a brightness temperature of less than 263 K. In the rainfall region, the lowest brightness

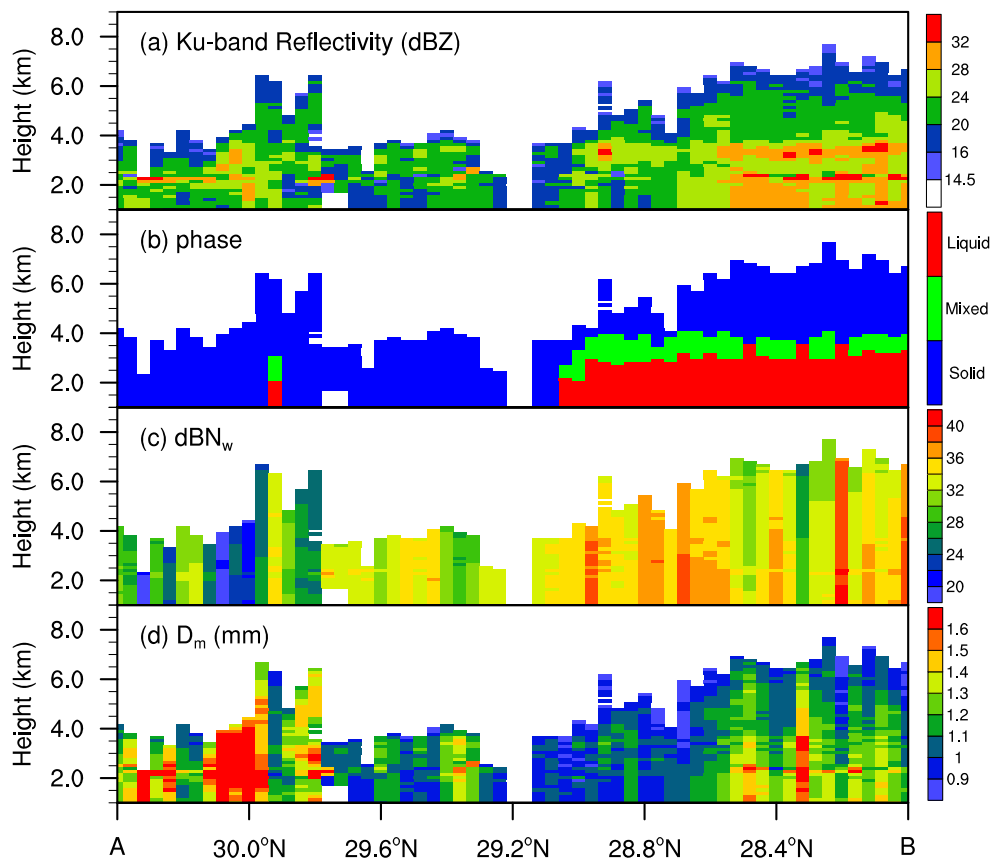


Figure 2. Vertical cross-sections along the AB line in Figure 1b: (a) Ku-band reflectivity, (b) precipitation phase, (c) droplet density (dBwN), and (d) effective droplet diameter (D_m).

temperature was even less than 220 K, showing that the highest cloud top was there. The distribution features of the brightness temperature indicate the existence of clouds at multiple heights, which ensures the representativeness of the retrieved R_e vertical evolution. In addition, Figure 1d presents the retrieved R_e using the BSR method. R_e reached 30 μm in the top and bottom right of the study region, while it was less than 12 μm in the bottom left and middle.

For detailed insight into the precipitation microphysics within this event, we carried out cross-section analysis along the AB line in Figure 1b. The AB line was taken from the 5th pixels of MS swaths (the 17th pixels of NS swaths). As shown in Figure 2, precipitation pixels along the AB line can be divided into two regions. In the top region (left in Figure 2), the Ku-band echo-top height was mostly 4–6 km, with the strongest echo about 24–28 dBZ (Figure 2a). These precipitation pixels were dominated by snowfall, and the droplet phase did not change vertically (Figure 2b).

In the bottom region of the AB line (right in Figure 2), the echo top reached about 6–8 km (Figure 2a). There were obvious bright bands in the vertical profiles, indicating stratiform precipitation. The near-surface precipitation was mainly liquid, while the melting layer was about 2.5–4 km (Figure 2b). Generally, due to the changes of volume and surface features of droplets during melting, droplet reflectivity reaches its strongest at some time within the melting process, which corresponds to the single bright band in the reflectivity profile (Sánchez-Diezma et al., 2000; Zhang & Fu, 2018). However, there were two bright bands in the reflectivity profile of the lower region (Figure 2a), which might be due to the existence of an atmospheric inversion layer at 1–3 km height (Figure S2), in which droplets may condense again after melting.

Correspondingly, Figures 2c and 2d show cross-sections of DSD parameters provided by dual-frequency algorithms, where dBwN represents droplet density and D_m is the effective droplet diameter. Droplet

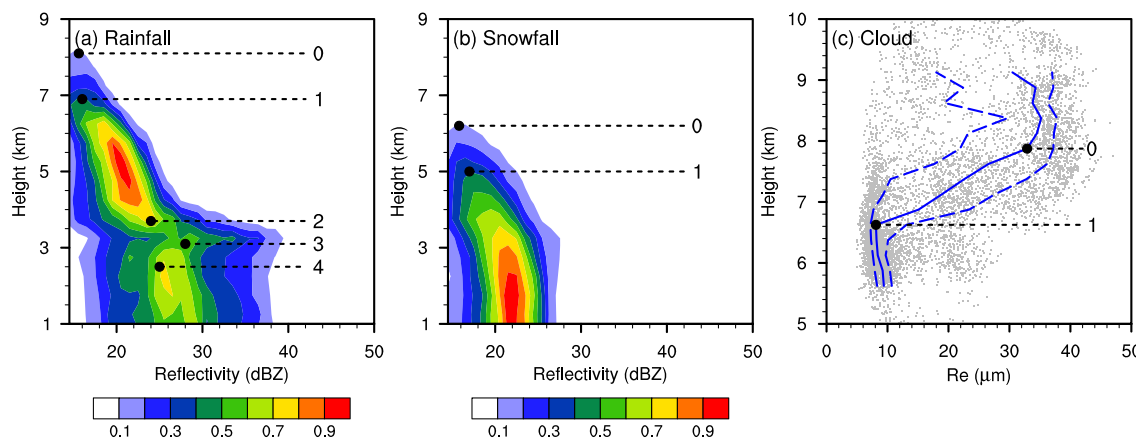


Figure 3. CFAD distributions of Ku-band reflectivity for (a) rainfall pixels and (b) snowfall pixels and (c) the derived R_e vertical evolution in the study region. The labels 0–4 indicate the turning points in the figures. The three lines in Figure 3c are, respectively, 25th, 50th, and 75th percentiles of R_e at each 0.25 km interval.

density of snowfall in the upper region was significantly lower than that of rainfall in the lower region because of the colder and drier environment behind the cold front (Naud et al., 2015).

For the surface precipitation phase, we divided the radar observations into two categories, rainfall and snowfall, and conducted contoured frequency by altitude diagrams (CFADs) of their Ku-band reflectivity (Yuter & Houze, 1995). Each CFAD was normalized by its overall maximum at a horizontal interval of 1 dBZ and a vertical interval of 0.25 km. Compared with normalization by level maximums (McMurdie et al., 2018), this method is more suitable for comparing results at different heights (Zagrodnik et al., 2019; Zhang et al., 2018).

The rainfall CFAD (Figure 3a) showed typical stratiform characteristics with five obvious turning points (marked as 0–4), which correspond to the boundaries of different microphysical processes. In stratiform precipitations, the vertical air motion is generally small compared with fall velocities of precipitation droplets (Houze, 1981). Precipitation droplets undergo various microphysical processes during dropping and eventually fall to the ground. The top zone from 0 to 1 corresponds to the deposition growth of ice droplets, which is the slowest microphysical growth mode. The microphysical process that occurs in this zone is also called the Bergeron–Findeisen process, by which ice crystals form precipitation droplets and slowly grow by “grabbing” water vapor from water crystals (Bergeron, 1935; Korolev, 2007). In the layer between 1 and 2, ice droplets continue to grow by deposition, riming, and aggregation. The riming process, by which ice droplets directly collect cloud water which freezes on contact, significantly accelerates the growth rate of precipitation droplets (Rutledge & Hobbs, 1983). The zone from 2 to 4 is where the melting process of precipitation droplets occurs. There was a clear bright band in this zone (Figure 3a), which indicated the most prominent feature of stratiform precipitation (Mason, 1972).

The snowfall CFAD (Figure 3b) is similar to that for rainfall above the melting layer. There was no bright band in snowfall’s CFAD, since ice droplets fall to the ground without melting. The deposition layer (points 0–1) in snowfall’s CFAD at 5–6.25 km is 2 km lower but equally as thick as that for rainfall at 7–8.25 km. When ice droplets fell below 5 km, the change of reflectivity accelerated, due to riming and aggregation processes. The reflectivity no longer increased with height below 3 km, indicating that precipitation droplets had left the cloud.

The corresponding R_e vertical evolution over the study region is shown in Figure 3c. Because cloud particles develop from cloud base to top, R_e increases with height, with the increase rate influenced by various cloud microphysics. Rosenfeld and Lensky (1998) divided R_e vertical evolution into five distinct vertical zones from cloud base to top, namely, diffusional growth zone, coalescence droplet zone, rainout zone, mixed-phase zone, and glaciated zone. These zones do not all necessarily exist in a given cloud system, and sometimes they may also overlap with each other (Rosenfeld & Lensky, 1998). In this case, there were three vertical cloud zones divided by two turning points (marked 0 and 1 in Figure 3c). The cloud particles in different zones were of different size and phase properties, which showed impressive consistency within the precipitation partitions.

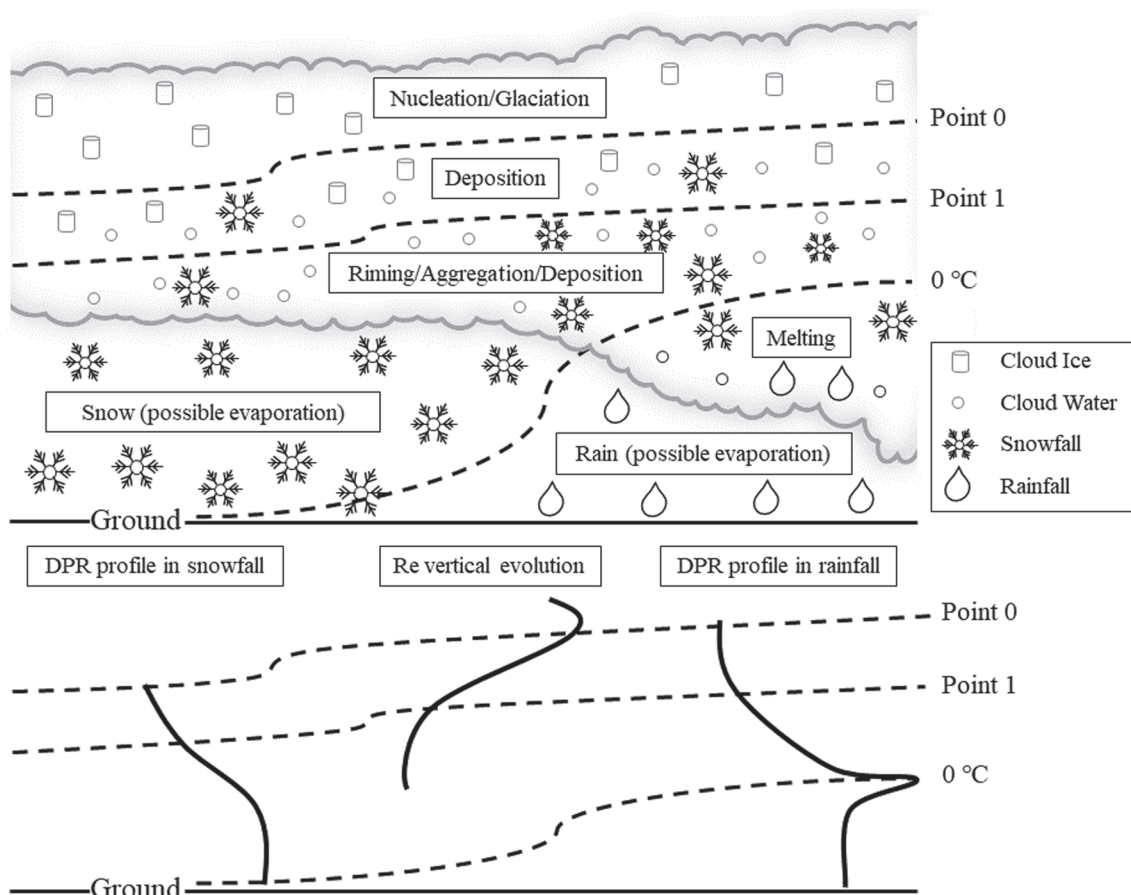


Figure 4. Conceptual diagram of cloud and precipitation particles within this event.

The cloud zone below point 1 is the diffusional growth zone (Figure 3c) at the cloud base; the mean R_e here was about $10 \mu\text{m}$, which hardly changed with height. Cloud particles in this zone are completely liquid including overcooled cloud water, which provides a favorable cloud environment for the riming growth of precipitation droplets (Wang & Ji, 2000).

The cloud zone between points 1 and 0 is the mixed-phase zone (Figure 3c); R_e changed rapidly with height from 10 to $34 \mu\text{m}$. The coexistence of cloud ice and cloud water in this zone is conducive to the formation of precipitation droplets, which corresponds to the Bergeron–Findeisen process and deposition growth of precipitation droplets (Bergeron, 1935). The cloud layer above point 0 is the glaciated zone, where hardly any cloud water exists and which is inconducive to the formation or growth of precipitation droplets.

4. Discussion

The consistency of cloud zones with precipitation partitions could be additionally verified by the numerical heights of the turning points. Each turning point of the R_e vertical evolution was exactly located between the corresponding turning points in the CFADs of rainfall and snowfall. The height of point 0 was 6.25 , 7.75 , and 8.25 km for snowfall's CFAD, R_e vertical evolution, and rainfall's CFAD, respectively, and 5 , 6.75 , and 7 km for point 1.

Synergistic application of passive and active satellite sensors shows unique advantages in the research of in-cloud microphysical processes. Previous studies have pointed out that aerosol invigorates cold rain and suppresses warm rain (e.g., Guo et al., 2018). Here, affected by air pollution aerosols, R_e maintains $\sim 10 \mu\text{m}$ up to 6.75 km , suppressing rain initiation (strong suppression of warm rain) below this height. The rapid increase of R_e between point 1 and point 0 makes the cloud water available for the formation of

mixed-phase precipitation. The cloud particle size retrieved by the passive sensor is also critical. If R_e is still 10 μm at the homogeneous ice nucleation temperature, there will be no effective mechanism for precipitation formation process (Rosenfeld, Liu, et al., 2014). Figure 3c shows that the R_e of this event reaches 34 μm before glaciation, which is undoubtedly beneficial to precipitation formation. If only the active sensor was used, it would be a challenge to recognize the intermediary role of cloud microphysics in the aerosol-cloud-precipitation interaction.

In contrast, passive sensor can only measure information on the cloud surface (Chen et al., 2019). Even if the vertical evolution of R_e can be obtained through appropriate assumptions, the structure at low level is still unknown. After introducing the active sensor, in-cloud microphysics below point 1 including riming, aggregation, melting, landfall, and possible evaporation can be clearly seen in Figures 3a and 3b. By combining active and passive sensors, a panoramic view of the microphysical processes was given simultaneously, including the vertical evolution of cloud particles from the bottom up and the formation and growth of precipitation droplet from the top down.

5. Conclusions

These results are summarized in the conceptual diagram in Figure 4. As the cold front passed through our study region (Figure S1), the low-level temperature changed drastically with the horizontal gradient exceeding 10°C/100 km. The R_e vertical evolution and DPR profiles showed two comparable turning points (marked 0 and 1). Above point 0, the cloud microphysics is dominated by glaciation and nucleation. Cloud water is completely frozen in this zone, which is inconducive for the formation of precipitation-size droplets. The area between points 0 and 1 is the mixed zone with coexisting cloud ice and cloud water. Ice precipitation droplets begin to form and slowly grow here due to deposition (the Bergeron–Findeisen process). Below point 1, cloud water dominates, and the zone provides a favorable environment for the riming growth of precipitation droplets. R_e hardly changed with height, while radar echo increased rapidly with decreasing altitude. Subsequent precipitation processes including melting and landfall are located at lower altitudes and often outside the clouds and therefore less related to cloud particles.

The development of China's new generation of geostationary satellites will provide observational basis for real-time weather monitoring and early warning systems (Yang et al., 2017). This study shows that the derived R_e vertical evolution from geostationary observations can be used to identify the zones of different cloud microphysics. Continuous spatial-temporal observation of the vertical evolution of clouds may also provide information for determining the existence and height of supercooled water in cloud (Figures S3–S5).

Data Availability Statement

The GPM 2ADPR precipitation data used in this study were collected from the Precipitation Measurement Mission website (<https://pmm.nasa.gov>). The ERA5 reanalysis data used in this study were collected from the ECMWF website (<https://apps.ecmwf.int/>). The FY-4A AGRI data used in this study were collected from the FENGYUN Satellite Data Center (<http://data.nsmc.org.cn/>).

Acknowledgments

This work was supported by the Key Research and Development Projects in Guangdong Province (grant number 2019B111101002), the Fundamental Research Funds for the Guangzhou Science and Technology Plan Project (grant number 20193010036), National Natural Science Foundation of China (grant numbers 41675043, 41775094, and 41405048), and the Fundamental Research Funds for the Central Universities (grant numbers 18lgpy07, 20lgpy19, and 20lgpy27).

References

- Ansmann, A., Tesche, M., Althausen, D., Müller, D., Seifert, P., Freudenthaler, V., et al. (2008). Influence of Saharan dust on cloud glaciation in southern Morocco during the Saharan mineral dust experiment. *Journal of Geophysical Research*, 113, D04210. <https://doi.org/10.1029/2007JD008785>
- Awaka, J., Iguchi, T., & Okamoto, K. (2009). TRMM PR standard algorithm 2A23 and its performance on bright band detection. *Journal of the Meteorological Society of Japan*, 87A, 31–52. <https://doi.org/10.2151/jmsj.87A.31>
- Bergeron, T. (1935). On the physics of cloud and precipitation. In: Proceedings of the 5th assembly, U.G.G.I., Lisbon. Vol. 2. p. 156.
- Caliskan, F., & Hajiyev, C. (2013). A review of in-flight detection and identification of aircraft icing and reconfigurable control. *Progress in Aerospace Sciences*, 60, 12–34. <https://doi.org/10.1016/j.paerosci.2012.11.001>
- Campos Braga, R., Rosenfeld, D., Weigel, R., Jurkat, T., Andreae, M. O., Wendisch, M., et al. (2017). Further evidence for CCN aerosol concentrations determining the height of warm rain and ice initiation in convective clouds over the Amazon basin. *Atmospheric Chemistry and Physics*, 17(23), 14,433–14,456. <https://doi.org/10.5194/acp-17-14433-2017>
- Chen, D., Guo, J., Yao, D., Lin, Y., Zhao, C., Min, M., et al. (2019). Mesoscale convective systems in the Asian monsoon region from advanced Himawari imager: Algorithms and preliminary results. *Journal of Geophysical Research: Atmospheres*, 124, 2210–2234. <https://doi.org/10.1029/2018JD029707>
- Chen, Y., Chen, G., Cui, C., Zhang, A., Wan, R., Zhou, S., et al. (2020). Retrieval of the vertical evolution of the cloud effective radius from the Chinese FY-4 (Feng Yun 4) next-generation geostationary satellites. *Atmospheric Chemistry and Physics*, 20(2), 1131–1145. <https://doi.org/10.5194/acp-20-1131-2020>

- Chen, Y., & Fu, Y. (2018). Tropical echo-top height for precipitating clouds observed by multiple active instruments aboard satellites. *Atmospheric Research*, 199, 54–61. <https://doi.org/10.1016/j.atmosres.2017.08.008>
- Fu, Y. (2014). Cloud parameters retrieved by the bispectral reflectance algorithm and associated applications. *Journal of Meteorological Research*, 28(5), 965–982. <https://doi.org/10.1007/s13351-014-3292-3>
- Geer, A. J., Baordo, F., Bormann, N., Chambon, P., English, S. J., Kazumori, M., et al. (2017). The growing impact of satellite observations sensitive to humidity, cloud and precipitation. *Quarterly Journal of the Royal Meteorological Society*, 143(709), 3189–3206. <https://doi.org/10.1002/qj.3172>
- Guo, J., Liu, H., Li, Z., Rosenfeld, D., Jiang, M., Xu, W., et al. (2018). Aerosol-induced changes in the vertical structure of precipitation: A perspective of TRMM precipitation radar. *Atmospheric Chemistry and Physics*, 18(18), 13,329–13,343. <https://doi.org/10.5194/acp-18-13329-2018>
- Houze, R. A. (1981). Structures of atmospheric precipitation systems: A global survey. *Radio Science*, 16(5), 671–689. <https://doi.org/10.1029/RS016i005p00671>
- Houze, R. A., Rasmussen, K. L., Zuluaga, M. D., & Brodzik, S. R. (2015). The variable nature of convection in the tropics and subtropics: A legacy of 16 years of the Tropical Rainfall Measuring Mission satellite. *Reviews of Geophysics*, 53, 994–1021. <https://doi.org/10.1002/2015RG000488>
- Iguchi, T., Seto, S., Meneghini, R., Yoshida, N., Awaka, J., Kubota, T., et al. (2012). An overview of the precipitation retrieval algorithm for the dual-frequency precipitation radar (DPR) on the global precipitation measurement (GPM) mission's core satellite. *Proceedings of SPIE*, 8528, 85281C. <https://doi.org/10.1117/12.977352>
- King, N. J., & Vaughan, G. (2012). Using passive remote sensing to retrieve the vertical variation of cloud droplet size in marine stratus-cumulus: An assessment of information content and the potential for improved retrievals from hyperspectral measurements. *Journal of Geophysical Research*, 117, D15206. <https://doi.org/10.1029/2012JD017896>
- Korolev, A. (2007). Limitations of the wegener-bergeron-findeisen mechanism in the evolution of mixed-phase clouds. *Journal of the Atmospheric Sciences*, 64(9), 3372–3375. <https://doi.org/10.1175/JAS4035.1>
- Lensky, I. M., & Rosenfeld, D. (2006). The time-space exchangeability of satellite retrieved relations between cloud top temperature and particle effective radius. *Atmospheric Chemistry and Physics*, 6(10), 2887–2894. <https://doi.org/10.5194/acp-6-2887-2006>
- Mason, B. J. (1972). The Bakerian Lecture, 1971. The physics of the thunderstorm. *Proceedings of the Royal Society of London. Series A: Mathematical and Physical Sciences*, 327(1571), 433–466. <https://doi.org/10.1098/rspa.1972.0056>
- McMurdie, L. A., Rowe, A. K., Houze, R. A., Brodzik, S. R., Zagrodnik, J. P., & Schuldt, T. M. (2018). Terrain-enhanced precipitation processes above the melting layer: Results from OLYMPEX. *Journal of Geophysical Research: Atmospheres*, 123, 12,194–12,209. <https://doi.org/10.1029/2018JD029161>
- Min, M., Wu, C., Li, C., Liu, H., Xu, N., Wu, X., et al. (2017). Developing the science product algorithm testbed for Chinese next-generation geostationary meteorological satellites: Fengyun-4 series. *Journal of Meteorological Research*, 31(4), 708–719. <https://doi.org/10.1007/s13351-017-6161-z>
- Naud, C. M., Posselt, D. J., & van den Heever, S. C. (2015). A CloudSat-CALIPSO view of cloud and precipitation properties across cold fronts over the global oceans. *Journal of Climate*, 28(17), 6743–6762. <https://doi.org/10.1175/JCLI-D-15-0052.1>
- Platnick, S. (2000). Vertical photon transport in cloud remote sensing problems. *Journal of Geophysical Research*, 105(D18), 22,919–22,935. <https://doi.org/10.1029/2000JD900333>
- Rosenfeld, D., Andreae, M. O., Asmi, A., Chin, M., De Leeuw, G., Donovan, D. P., et al. (2014). Global observations of aerosol-cloud-precipitation-climate interactions. *Reviews of Geophysics*, 52, 750–808. <https://doi.org/10.1002/2013RG000441>
- Rosenfeld, D., Fromm, M., Trentmann, J., Luderer, G., Andreae, M. O., & Servranckx, R. (2007). The Chisholm firestorm: Observed microstructure, precipitation and lightning activity of a pyro-cumulonimbus. *Atmospheric Chemistry and Physics*, 7(3), 645–659. <https://doi.org/10.5194/acp-7-645-2007>
- Rosenfeld, D., & Lensky, I. M. (1998). Satellite-based insights into precipitation formation processes in continental and maritime convective clouds. *Bulletin of the American Meteorological Society*, 79(11), 2457–2476. [https://doi.org/10.1175/1520-0477\(1998\)079<2457:SBIIPF>2.0.CO;2](https://doi.org/10.1175/1520-0477(1998)079<2457:SBIIPF>2.0.CO;2)
- Rosenfeld, D., Liu, G., Yu, X., Zhu, Y., Dai, J., Xu, X., & Yue, Z. (2014). High-resolution (375 m) cloud microstructure as seen from the NPP/VIIRS satellite imager. *Atmospheric Chemistry and Physics*, 14(5), 2479–2496. <https://doi.org/10.5194/acp-14-2479-2014>
- Rosenfeld, D., & Woodley, W. L. (2003). Closing the 50-year circle: From cloud seeding to space and back to climate change through precipitation physics. In: Tao, WeiKuo, Adler, Robert (Eds.), *Cloud systems, hurricanes, and the Tropical Rainfall Measuring Mission (TRMM)* (pp. AMS, Boston. 234 p, pp. 59–80, meteorological monographs 51 (Chapter 6).
- Rudich, Y., Khersonsky, O., & Rosenfeld, D. (2002). Treating clouds with a grain of salt. *Geophysical Research Letters*, 29(22), 2060. <https://doi.org/10.1029/2002GL016055>
- Rutledge, S. A., & Hobbs, P. V. (1983). The mesoscale and microscale structure and organization of clouds and precipitation in midlatitude cyclones. VIII. A model for the ‘seeder-feeder’ process in warm-frontal rainbands. *Journal of the Atmospheric Sciences*, 40(5), 1185–1206. [https://doi.org/10.1175/1520-0469\(1983\)040<1185:TMAMSA>2.0.CO;2](https://doi.org/10.1175/1520-0469(1983)040<1185:TMAMSA>2.0.CO;2)
- Sánchez-Diezma, R., Zawadzki, I., & Semper-Torres, D. (2000). Identification of the bright band through the analysis of volumetric radar data. *Journal of Geophysical Research*, 105(D2), 2225–2236. <https://doi.org/10.1029/1999JD900310>
- Stephens, G. L., Vane, D. G., Boain, R. J., Mace, G. G., Sassen, K., Wang, Z., et al. (2002). The cloudsat mission and the A-Train: A new dimension of space-based observations of clouds and precipitation. *Bulletin of the American Meteorological Society*, 83(12), 1771–1790. <https://doi.org/10.1175/BAMS-83-12-1771>
- Stephens, G. L., Vane, D. G., Tanelli, S., Im, E., Durden, S., Rokey, M., et al. (2008). CloudSat mission: Performance and early science after the first year of operation. *Journal of Geophysical Research*, 113, D00A18. <https://doi.org/10.1029/2008JD009982>
- Sun, Z., Thilakavathy, K., Kumar, S. S., He, G., & Liu, S. V. (2020). Potential factors influencing repeated SARS outbreaks in China. *International Journal of Environmental Research and Public Health*, 17(5), 1633. <https://doi.org/10.3390/ijerph17051633>
- Wang, P. K., & Ji, W. (2000). Collision efficiencies of ice crystals at low-intermediate Reynolds numbers colliding with supercooled cloud droplets: A numerical study. *Journal of the Atmospheric Sciences*, 57(8), 1001–1009. [https://doi.org/10.1175/1520-0469\(2000\)057<1001:CEOICA>2.0.CO;2](https://doi.org/10.1175/1520-0469(2000)057<1001:CEOICA>2.0.CO;2)
- Winker, D. M., Vaughan, M. A., Omar, A., Hu, Y., Powell, K. A., Liu, Z., et al. (2009). Overview of the CALIPSO mission and CALIOP data processing algorithms. *Journal of Atmospheric and Oceanic Technology*, 26(11), 2310–2323. <https://doi.org/10.1175/2009JTECHA1281.1>
- Woodley, W. L., Rosenfeld, D., Kelman, G., & Golden, J. H. (2008). Short-term forecasting of severe convective storms using quantitative multi-spectral, satellite imagery: Results of the early alert project. In: 24th Conference on Severe Local Storms, 27–31 October 2008, Savannah, Georgia.

- Yang, J., Zhang, Z., Wei, C., Lu, F., & Guo, Q. (2017). Introducing the new generation of Chinese geostationary weather satellites, Fengyun-4. *Bulletin of the American Meteorological Society*, 98(8), 1637–1658. <https://doi.org/10.1175/BAMS-D-16-0065.1>
- Yuter, S. E., & Houze, R. A. (1995). 3-dimensional kinematic and microphysical evolution of Florida cumulonimbus. Part II: Frequency-distributions of vertical velocity, reflectivity, and differential reflectivity. *Monthly Weather Review*, 123, 1941–1963. [https://doi.org/10.1175/1520-0493\(1995\)123<1941:TDKAME>2.0.CO;2](https://doi.org/10.1175/1520-0493(1995)123<1941:TDKAME>2.0.CO;2)
- Zagrodnik, J. P., McMurdie, L. A., Houze, R. A., & Tanelli, S. (2019). Vertical structure and microphysical characteristics of frontal systems passing over a three-dimensional coastal mountain range. *Journal of the Atmospheric Sciences*, 76(6), 1521–1546. <https://doi.org/10.1175/JAS-D-18-0279.1>
- Zhang, A., & Fu, Y. (2018). Life cycle effects on the vertical structure of precipitation in East China measured by Himawari-8 and GPM DPR. *Monthly Weather Review*, 146(7), 2183–2199. <https://doi.org/10.1175/MWR-D-18-0085.1>
- Zhang, A., Fu, Y., Chen, Y., Liu, G., & Zhang, X. (2018). Impact of the surface wind flow on precipitation characteristics over the southern Himalayas: GPM observations. *Atmospheric Research*, 202, 10–22. <https://doi.org/10.1016/j.atmosres.2017.11.001>
- Zheng, Y., & Rosenfeld, D. (2015). Linear relation between convective cloud base height and updrafts and application to satellite retrievals. *Geophysical Research Letters*, 42, 6485–6491. <https://doi.org/10.1002/2015GL064809>